

$^{12}\text{C}(\alpha,\gamma)^{16}\text{O}$ cross sections at stellar energies

J. M. L. Ouellet,* M. N. Butler,† H. C. Evans, H. W. Lee, J. R. Leslie, J. D. MacArthur, W. McLatchie, H.-B. Mak, P. Skensved, J. L. Whitton, and X. Zhao
Queen's University, Kingston, Ontario, Canada K7L 3N6

T. K. Alexander‡

Atomic Energy of Canada Limited, Chalk River, Ontario, Canada K0J 1J0

(Received 21 June 1996)

The excitation function of the $^{12}\text{C}(\alpha,\gamma)^{16}\text{O}$ reaction and the angular distribution of its γ rays were measured at nine center-of-mass energies ranging from $E=1.37$ to 2.98 MeV. These measurements allowed the separation of the $E1$ and $E2$ contributions and their extrapolation to the region of astrophysical interest. The analysis of all the available $E1$ cross sections with the K -matrix method and with a three-level R -matrix method yields a consistent prediction of 79 ± 16 keV b for the $E1$ S factor at 300 keV. The $E2$ contribution at the same energy is 36 ± 6 keV b from a cluster model analysis of the present data. The best estimate of the total S factor at 300 keV is 120 keV b, and it is unlikely that it will fall outside the range of 80–160 keV b. [S0556-2813(96)05410-6]

PACS number(s): 25.55.-e, 26.20.+f, 27.20+n, 95.30.Cq

I. INTRODUCTION

In the helium-burning phase of stellar evolution, the two important reactions are $3\alpha\rightarrow^{12}\text{C}$ and $^{12}\text{C}(\alpha,\gamma)^{16}\text{O}$. The cross section for $^{16}\text{O}(\alpha,\gamma)^{20}\text{Ne}$, the next possible link in the helium-burning chain, is too small at the temperatures encountered here (near 2×10^8 K [3]) for this reaction to be significant. The relative rates of $3\alpha\rightarrow^{12}\text{C}$ and $^{12}\text{C}(\alpha,\gamma)^{16}\text{O}$ determine the $^{12}\text{C}/^{16}\text{O}$ ratio at the end of helium burning and have a major effect on subsequent stages of stellar evolution [1,2]. The rate of the first reaction is known to $\sim 15\%$. By contrast, there has been for a long time a substantial uncertainty in the cross section of $^{12}\text{C}(\alpha,\gamma)^{16}\text{O}$ in spite of extensive work extending over several decades.

The difficulty in determining the $^{12}\text{C}(\alpha,\gamma)^{16}\text{O}$ reaction rate is due principally to the extremely small value of the cross section and the presence of substantial γ -ray background. At 300 keV (the mean interaction energy)¹ the cross section is on the order of 10^{-17} b, seven orders of magnitude smaller than at 1 MeV, the lowest energy for which measurements have been reported [4]. The major energy dependence of astrophysical reaction rates is customarily factored out of the cross section by defining the astrophysical S factor

$$S(E) = E\sigma(E)\exp(2\pi\eta), \quad (1)$$

where E is the center-of-mass energy, $2\pi\eta=2\pi Z_1 Z_2 e^2/\hbar v$, and v is the relative velocity of the two nuclei (of charge Z_1 and Z_2) taking part in the reaction. The extrapolation of the S

factor to low energy is complicated by the presence of two ^{16}O subthreshold levels, a $J^\pi=1^-$ state near the threshold at -45 keV and a 2^+ state farther away at -245 keV. An energy level diagram is shown in Fig. 1. The measured cross sections are only slightly sensitive to these levels and are dominated by a broad 1^- state at 2.42 MeV and by direct electric quadrupole ($E2$) radiative capture, while the cross section at 300 keV is expected to be dependent on the nearby subthreshold $J^\pi=1^-$ level and to some extent also the subthreshold $J^\pi=2^+$ level. The major source of background is neutron capture γ rays following the strong reaction $^{13}\text{C}(\alpha,n)$, and to reduce it, separated isotope ^{12}C targets, time-of-flight techniques, and ^{12}C beams on ^4He gas targets have all been used. In addition, care is required to prevent carbon buildup on apertures or the targets and to suppress background from cosmic rays.

The $^{12}\text{C}(\alpha,\gamma)^{16}\text{O}$ S factor at the energy of interest, $S(300)$, is inaccessible to direct measurement. To obtain its value, the conventional approach is to perform a measurement of the excitation function down to the lowest possible energy and extrapolate it to 300 keV. That extrapolation must be performed separately for the electric dipole ($E1$) and electric quadrupole ($E2$) components, which have different energy dependence. The separation of the two contributions requires at each energy the ratio of cross sections σ_{E1}/σ_{E2} , which is ideally, obtained from the angular distribution of the reaction γ rays. To reduce the uncertainty introduced by the extrapolation, the results of $^{12}\text{C}(\alpha,\alpha)^{12}\text{C}$ elastic scattering experiments are included in the analysis. The extrapolated values of $S(300)$ obtained in a number of experiments remained poorly determined and do not agree well with one another [6–9].

A precise measurements of the α -particle spectrum following the β decay of ^{16}N has been reported recently by Azuma *et al.* [10] Their α width for the 1^- level is substantially lower than the value deduced by Plaga *et al.* [5] from $l=1$ phase shift analysis of elastic scattering data which is not sensitive to this α width. When the ^{16}N data were included in the analysis of the $E1$ cross section, they provided

*Permanent address: Centre universitaire de sant  de l'Estrie, Sherbrooke, Qu bec, Canada J1H 5N4.

†Permanent address: Department of Astronomy and Physics, St. Mary's University, Halifax, Nova Scotia, Canada B3H 3C3.

‡Permanent address: Box 1634, 83 Frontenac Cres., Deep River, Ontario, Canada K0J 1P0.

¹We use center-of-mass energies throughout this paper.

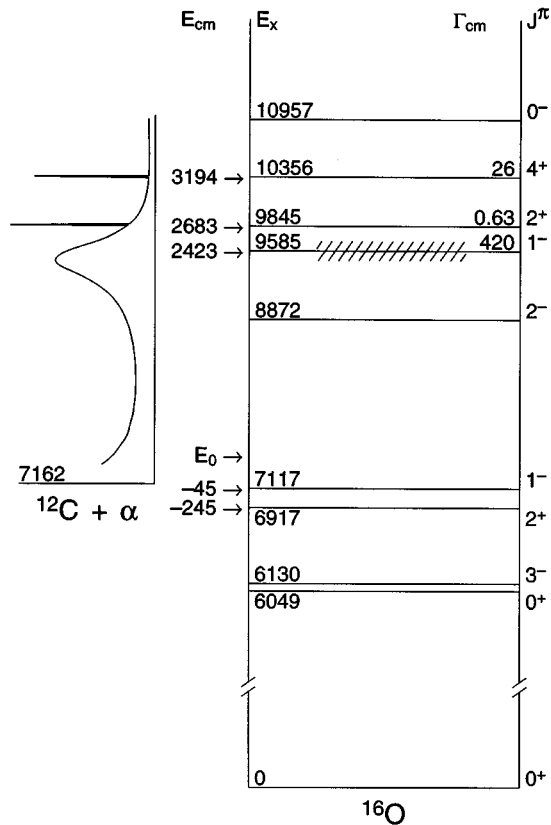


FIG. 1. Partial level scheme for ^{16}O . Also shown are the center-of-mass energy $E_{\text{c.m.}}$, the width $\Gamma_{\text{c.m.}}$, and the spin parity J^π of some of the states, as well as a schematic representation of the $^{12}\text{C}(\alpha,\gamma)^{16}\text{O}$ S factor. Energies are in keV.

a strong constraint on the α width of the 1^- subthreshold state and resulted in a much reduced uncertainty in the $E1$ astrophysical S factor at 300 keV, $S_{E1}(300)$. The results of the R -matrix and K -matrix analysis of the complete data set [4–6,8–10] for $S_{E1}(300)$ gave values of 79 ± 21 and 82 ± 26 keV b, respectively. Recently, it has been suggested that a 1^- subthreshold echo pole may reduce the usefulness of K -matrix fits in restricting the acceptable range of $S_{E1}(300)$ [11]. Analyses performed separately for each of the σ_{E1} data sets resulted in a spread that is substantially less than the errors given above. With the constraint provided by the ^{16}N data, the systematic differences between the $^{12}\text{C}(\alpha,\gamma)^{16}\text{O}$ data sets would appear to be less important for the determination of $S_{E1}(300)$.

The subthreshold 2^+ level is not populated by the ^{16}N β decay. The only information on its reduced α width comes from the $l=2$ phase shift analysis of the elastic scattering data of Plaga *et al.* [5]. The phase shift data have large statistical variation in the region sensitive to the 2^+ α width and do not provide a constraint on its value.

We report here on a measurement of the $^{12}\text{C}(\alpha,\gamma)^{16}\text{O}$ cross section in which full angular distributions were measured at nine energies between 1.36 and 2.98 MeV. Six high-efficiency germanium detectors were used in fixed geometry at all energies and the targets were ^{12}C implanted in gold. The implanted carbon depletes slowly due to sputtering by the $^4\text{He}^+$ beam. The carbon depth profile in each target was measured before each run and periodically during long runs.

The $E1$ and $E2$ cross sections reported here depend on the experimental analysis only and are independent of models used in the extrapolations. The present values supersede those published earlier [9] which contain a mistake in the calculation of the effective target thickness. The following sections describe the experimental arrangement and procedure, the data analysis, the extrapolation of the $E1$ and $E2$ S factors, and the conclusions.

II. EXPERIMENTAL METHOD

A. Accelerator and beam transport

The $^4\text{He}^+$ beam for this experiment was produced by the Queen's University 4-MV Van de Graaff accelerator and beam currents between 20 μA and 35 μA were used. The reproducibility of the beam energy calibration was better than 1 keV, and the spread in the beam energy was less than 3 keV at all energies. Two beam profile monitors were mounted at distances of 0.5 and 1.9 m from the target, respectively. They allowed the beam position and focus to be monitored without introducing narrow slits, which could have been a source of background. A magnetic steerer, located 2.2 m from the target, was used to sweep the beam over the target. Asynchronous frequencies below 1 Hz were used to produce the horizontal and vertical deflections of the beam.

The 6 m of beam line closest to the target was constructed of stainless steel components and, with only a few exceptions, was coupled together with metal seals. A refrigerated section which included an in-line baffle was located above an oil diffusion pump, at the junction between the clean beam line and the rest of the beam transport system. It served to control the migration of hydrocarbon vapors towards the target. The rough pumping of the line was done with carbon vane and absorption pumps. A second in-line baffle, cooled with liquid nitrogen, was located 3 m from the target. A third cold trap was incorporated in the target chamber (Fig. 2). It was cooled with liquid nitrogen and surrounded the beam immediately in front of the target. A 350 L/s cryopump, located 0.7 m from the target, allowed a vacuum of 6×10^{-7} Torr to be maintained with the beam on target.

B. Target chamber

A vertical section of the target chamber is shown in Fig. 2. The target was held at an angle of 45° to the incident beam. Its copper backing was directly water cooled, and indium wire was used as a seal on both the vacuum and water sides. A ceramic insulator provided electrical isolation for the target chamber and allowed it to be used as a Faraday cup for beam current measurements. Leakage currents of a few tens of nanoamperes, due to the conductivity of the water cooling lines, were observed. The suppressor ring, 25 mm in front of the target, was kept at -500 V. It was supported on the upper half-cylindrical tube placed between the chamber wall and the cold trap. A 10-mm-diam collimator, mounted on the lower half-cylindrical tube, was located just in front of the suppressor ring. The amplitude of the beam sweep was limited so that occasional excursions of the collimator current did not exceed a few tens of nanoamperes. This resulted in a beam spot on the inclined target that typically measured

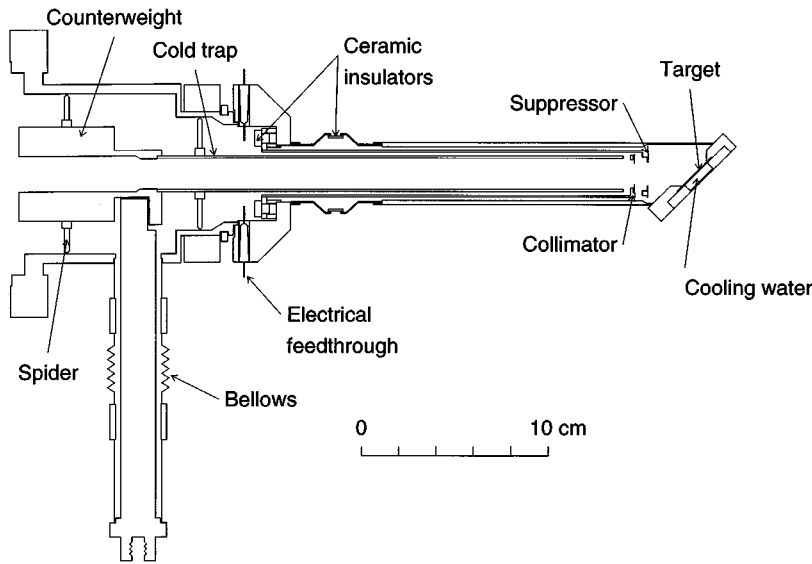


FIG. 2. Schematic diagram of the target holder for the present experiment. The setup included a nitrogen-cooled cylindrical cold trap, a single wide collimator, and an electron suppressor. The target was directly water cooled and electrically insulated to allow measurements of the beam current.

5 mm by 7 mm in the horizontal and vertical directions, respectively. The cylindrical cold trap and counterweight were made of copper and supported on two spiders. Cooling was provided through the vertical copper rod, which was immersed in liquid nitrogen. The bellows allowed for differential expansion.

C. Target preparation

Isotopically separated targets were prepared by implanting ^{12}C at an energy of 110 keV into a thick gold layer on a copper backing. The backings were 25-mm square copper sheets, 0.5 mm thick, on which thin layers of nickel and then gold were electroplated to assure good adhesion. High-purity gold (99.999%) was evaporated on top of the electroplated gold in a 16–18 mg/cm^2 layer, which was sufficiently thick to ensure that enough high-purity gold remained after target preparation to stop 4-MeV α particles.

The isotope ratio $^{13}\text{C}/^{12}\text{C}$ in the implanted targets was determined by comparing the γ -ray yield for the narrow resonance of the $^{13}\text{C}(p,\gamma)^{14}\text{N}$ reaction at $E_p=1.7475$ MeV with the yield from a natural carbon target. These measurements showed the ^{13}C content in the bulk of the targets to be reduced by three orders of magnitude to 1 part in 10^5 . However, a higher concentration of ^{13}C was noted on the surface. This proved not to be a problem since that contamination, present on newly made targets, disappeared after exposure to the ^4He beam for a few hours.

Each target was analyzed using Rutherford backscattering (RBS) to obtain the depth profile and total concentration of the implanted carbon. A 5-nA beam of 2-MeV ^4He ions was used, and the scattered particles were observed in a surface-barrier detector subtending 4 mrad placed at 156° . A typical RBS spectrum is shown in Fig. 3, along with a simulated spectrum calculated by the analysis program RUMP [12]. The simulation was generated assuming a mixture of carbon and gold which was adjusted empirically to reproduce the observed spectrum. The low-energy peak due to scattering from carbon was not useful as it was largely obscured by background from the gold. The sensitivity to the carbon depth profile was obtained from the reduction in yield near the

surface between channels 450 and 560. RBS spectra were obtained at a number of positions on the target to verify that the implantation was uniform over the area exposed to the beam. A total of nine targets was eventually used. Their carbon content varied between 3.0 and 5.0×10^{18} atom/cm^2 and the maximum C/Au ratio (by number) was close to 15:1 in most cases.

The RBS technique was also used to determine the thickness and integrity of the evaporated gold layer after the implantation. A beam of 3-MeV protons was needed to probe at the required depth. A sample RBS spectrum is shown as the jagged line in Fig. 4. The smooth line in the figure is the simulation for a layer of 17 mg/cm^2 of pure gold on top of pure copper. The sharpness of the low-energy edge of the gold signal is reasonably consistent with an absence of mixing between gold and copper if straggling is taken into account. The sharp peak on top of the gold plateau is due to the

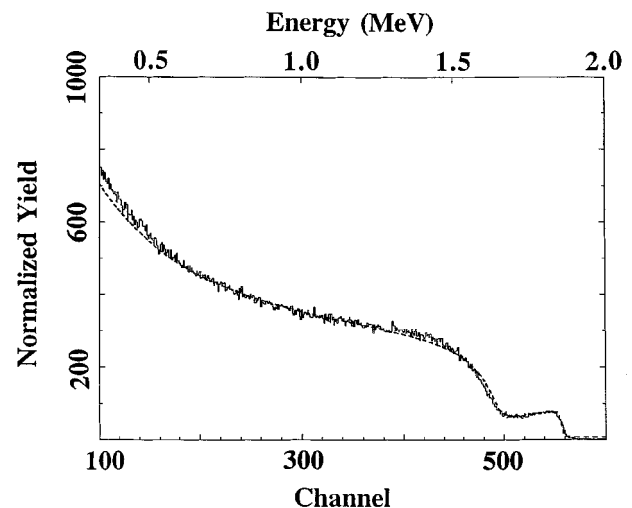


FIG. 3. A typical Rutherford backscattering spectrum produced by 2-MeV $^4\text{He}^+$ ions incident on a ^{12}C target implanted in gold observed with a surface barrier detector at 156° . The reduction in yield above 1.5 MeV is due to the implanted carbon.

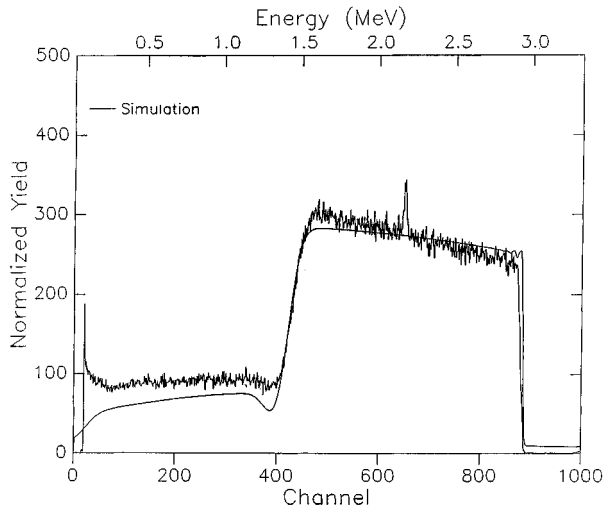


FIG. 4. A Rutherford backscattering spectrum produced by 3-MeV protons incident on a ^{12}C target implanted in gold evaporated on a copper backing. The sharp peak is due to scattering from carbon which also caused the reduced yield at the high-energy edge compared to the simulated data.

implanted carbon which also caused the depletion of counts at the high-energy edge compared to the simulated rate.

To monitor the state of the ^{12}C implant during the experiments, the γ -ray yield from the narrow $^{12}\text{C}(\alpha, \gamma)^{16}\text{O}$ 2^+ resonance at $E_\alpha = 3.58$ MeV was observed. This resonance was scanned for each newly installed target and at intervals of 2 or 3 days thereafter. The frequency of the scans was limited, as each required 6 to 8 h of beam time. The measured yield was the sum for all six detectors of the total counts in the 8.6–10.0 MeV region. Typical data are shown in Fig. 5. The solid line was obtained from a new target, and the other lines show the yields after exposure to the indicated charge of the 2.4-MeV ^4He beam.

The scans show that the surface of the target was sputtered away with little change in the concentration of carbon below the surface. The thickness of this target, expressed in

units of α -particle energy loss, decreased from just under 110 to 70 keV after a total incident charge of 11.5 C. The sputtering rate was higher than initially expected and was more rapid at the lower energies. After about 8–10 days of continuous use, a typical target would have lost 40% of its implanted carbon and was replaced.

D. Detectors

The reaction γ rays were detected in six large volume germanium detectors positioned to provide good sensitivity for the measurement of the angular distributions and the highest possible counter efficiency. Two detectors were placed at 90° to the incident beam 38 mm directly above and below the target center. The other four detectors surrounded the target in the horizontal plane as shown in Fig. 6. They were located at laboratory angles of 28° , 60° , 120° , and 143° , and distances of 50, 50, 60, and 80 mm, respectively. Detailed information is given in Table I. The detectors were shielded from room background by 45 mm of lead or an equivalent thickness of Kennurium alloy. The latter has a density 50% greater than Pb and is composed mainly of copper and tungsten; it was used in the congested region near the target. Six plastic scintillation counters were placed above the germanium detectors so that they subtended a solid angle close to 2π . A fast coincidence was formed between discriminator pulses fanned in from the scintillation counters on one side and from the germanium counters on the other. When such a coincidence occurred, the electronics generated a 10- μs blanking pulse to block all germanium signals. This technique insured identical dead time losses ($\approx 1.5\%$) in all detectors.

In a typical unshielded detector (the 60° counter), the beam-independent background was measured to be 56 counts/MeV/h in the energy range between 7 and 11 MeV in the Van de Graaff target room, which was constructed of low-activity concrete. The background for the same detector placed inside the shielding with the cosmic-ray veto system operating was 3 counts/MeV/h. The beam-dependent background was estimated by observing the counting rate in a

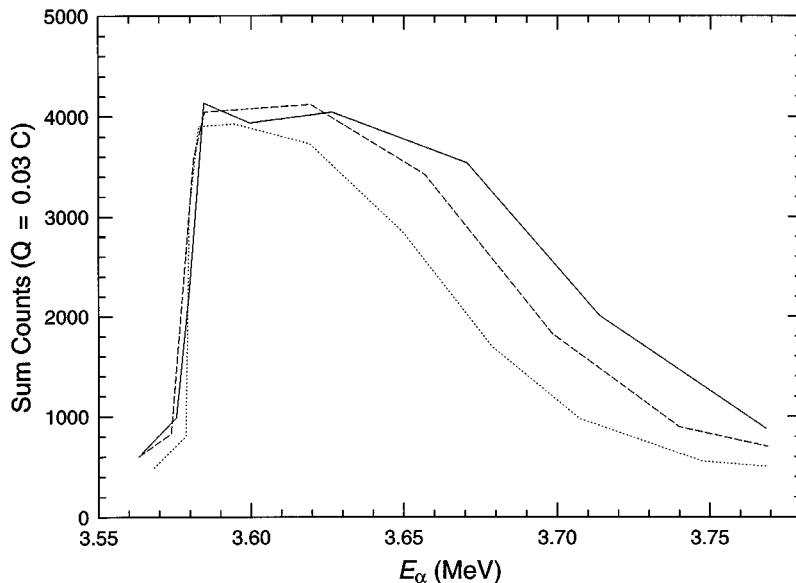


FIG. 5. Profile of carbon concentration in a target obtained from scans in which the γ -ray yield from the narrow $E_\alpha = 3.58$ MeV resonance was observed. The solid line was measured with the new target, while the dashed and dotted lines were obtained after charges of 4.71 and 11.52 C of α particles/h on the target.

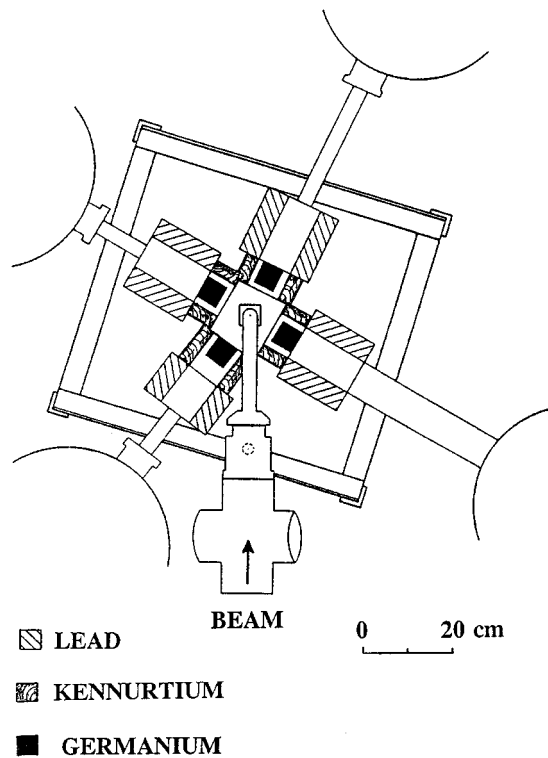


FIG. 6. Arrangement of the germanium detectors and shielding. The four detectors lying in the horizontal plane are shown. The 90° detectors located above and below the target are not shown.

1-MeV-wide window just above the energy of the ground-state transition in ^{16}O following α capture on ^{12}C . This rate increased with the beam energy and was 5 and 22 counts/MeV/h for a 30- μA ^4He beam used at $E_{\text{c.m.}}=1.4$ and 3.0 MeV, respectively.

The efficiencies of the detectors in the high-energy region were measured *in situ* with the $^{27}\text{Al}(p,\gamma)^{28}\text{Si}$ reaction at the $E_p=992$ keV resonance. The latter produces several γ rays situated between 1.8 and 10.8 MeV, whose relative intensities and angular distributions are known [13]. The photopeak and the escape peaks of all the strong lines were analyzed, and interpolations were done for the γ energies of interest. From the published resonance strength [14], absolute efficiencies were obtained, but only the more precise relative values were used in the present analysis. The overall normalization of the cross sections was done by using the yield at the broad 1^- resonance. The resulting cross sections were in

reasonable agreement with those computed from the measured efficiencies.

III. EXTRACTION OF THE CROSS SECTIONS

A. γ -ray spectra

Sixteen experimental runs were performed, totaling 1950 h of beam time, and covering nine nominal center-of-mass energies. (A run is to be understood as a continuous data-taking session, lasting typically for several days.) In each case, six γ -ray spectra were obtained. The gains of the detectors were always adjusted to reproduce the same dispersion (≈ 2.8 keV/channel).

In the low-energy region of the spectra ($E_\gamma < 3$ MeV), peaks were observed from inelastic neutron scattering on heavy nuclei, especially iron (from the stainless steel), lead (used for shielding), and copper (a constituent of the Kennurium alloy used for shielding) (Fig. 7). In particular, the line of ^{208}Pb at 2615 keV was quite prominent. Between 3 and 5 MeV, three γ rays caused by contaminants in the gold backing of the target were observed: two narrow lines at 3684 and 3854 keV from the $^{10}\text{B}(\alpha,n)^{13}\text{C}$ reaction and a wide peak at 4454 keV from $^9\text{Be}(\alpha,n)^{12}\text{C}$. None of these γ rays interfered directly with the peaks from the ground-state transition of $^{12}\text{C}(\alpha,\gamma)^{16}\text{O}$, which all appear above 7 MeV. The reaction $^9\text{Be}(\alpha,n)^{12}\text{C}$ was an important source of neutrons, whose capture in the vicinity of the target was presumably a significant contributor to the γ background.

The high-energy region of some of the spectra taken at 90° at all nine center-of-mass energies covered by the present experiment are shown on Fig. 8. (Sample spectra at other angles have been published previously [9].) Under the peaks of interest, the background was in general smooth and decreasing with increasing energy. The lines from the cascades through the levels at 6.917 and 7.117 MeV in ^{16}O were visible in many spectra, especially at the higher center-of-mass energies, in agreement with previous observations [4].

The energy of the γ ray from the ground-state transition of $^{12}\text{C}(\alpha,\gamma)^{16}\text{O}$ varied with the incident α -particle energy from $E_\gamma=8.6$ MeV at $E_{\text{c.m.}}=1.40$ MeV to $E_\gamma=10.2$ MeV at $E_{\text{c.m.}}=3.00$ MeV (Fig. 8). The full widths at half maximum (FWHM) of the peaks were between 70 and 110 keV; this was much larger than the combined contributions of the beam spread and the Ge detector resolution, which have FWHM of the order of 3 and 15 keV, respectively. The peak width was primarily due to the thickness of the target and, to a lesser extent, to the Doppler broadening that comes from

TABLE I. Characteristics of the γ -ray detectors.

Position	d_{fac}^a (cm)	d_{cr}^a (cm)	Rel. eff. (%)	Volume (cm^3)	Q_1	Q_2	Q_3	Q_4
28°	5.0	5.6	20	95	0.9719	0.9173	0.8395	0.7431
60°	5.0	5.5	30	145	0.9675	0.9047	0.8162	0.7081
90°	3.8	4.4	28	125	0.9541	0.8670	0.7474	0.6068
90°	3.8	4.3	30	140	0.9543	0.8675	0.7486	0.6091
120°	6.0	6.5	18	80	0.9762	0.9296	0.8627	0.7787
143°	8.0	8.6	30	130	0.9831	0.9500	0.9017	0.8400

^aDistances from the target center to the face of the detector and to the germanium crystal, respectively.

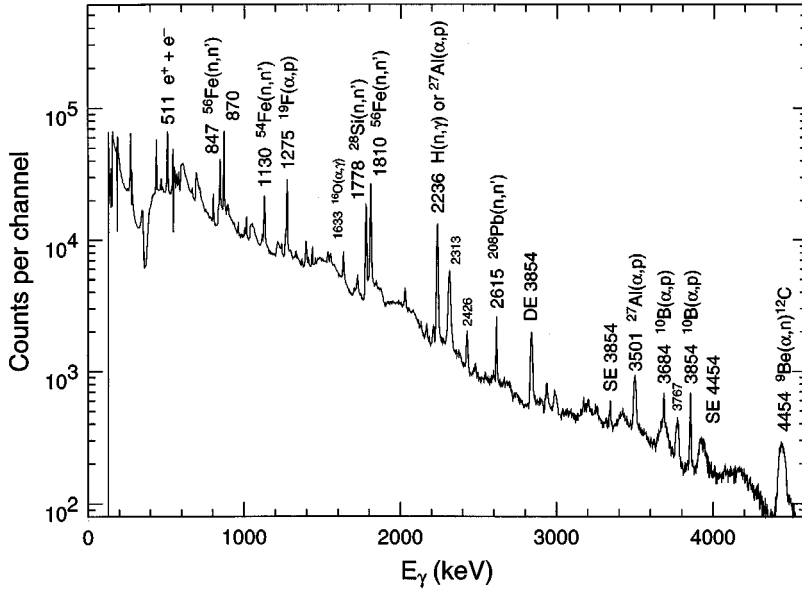


FIG. 7. Sample low-energy region of a spectrum obtained at 90° with an α beam of energy $E_\alpha=4.0$ MeV. The observed peaks come essentially from α -induced reactions on trace elements still present in the target (Al, B, Be, F) and inelastic neutron scattering on major constituents of the experimental setup (Fe in the beam pipes and Pb for the shielding).

the large solid angle subtended by the detectors. At most center-of-mass energies, substantially more counts were recorded at 90° than at the most forward and backward angles because the angular distribution was dominated by the $E1$

component, while a significant $E2$ admixture caused the yield at 60° to be larger than at 120° (Fig. 10).

B. Target thicknesses

The targets for the present work were in the form of ^{12}C implanted into gold backings. The relative concentration of ^{12}C and gold varied as a function of depth, and the target was continuously eroded by sputtering during the measurements. Periodic scans with the narrow resonance of $^{12}\text{C}(\alpha, \gamma)^{16}\text{O}$ at $E_\alpha=3.58$ MeV were used to measure the carbon concentration profile of the target. The scan data were γ -ray yields in the region $E_\gamma=8.6\text{--}10.0$ MeV (summed over the six germanium detectors) as a function of the incident beam energy (Fig. 5). Since the width of the 3.58-MeV resonance is only 0.6 keV, the incident α energy can be easily converted into a depth with the help of published energy loss tables [15]. The yield at each depth is proportional to the concentration of carbon and inversely proportional to the stopping power at that depth.

The scans performed at different times during a given run were combined to produce a charge-weighted or effective target density profile. Its energy steps and ^{12}C concentrations were scaled to account for the difference in the ratio of stopping powers of carbon versus gold between the energy of the scan ($E_\alpha=3.58$ MeV) and the energy of the current run ($E_\alpha=1.86\text{--}4.0$ MeV). Finally the energy scale was converted to the center-of-mass system. Integration of the profile yielded the effective target thickness. Over the course of the present work, the latter was found to lie within $\pm 40\%$ of an average of 3.6×10^{18} carbon atoms/cm 2 .

In the yield measurements, a single cross section (at the energy associated with the centroid of the γ -ray peaks) is to be extracted by fitting the observed γ -ray peaks with a calculated peak shape. In a situation where the cross section $\sigma(E)$ is constant and the detectors have perfect resolution, the effective target density profile would be exactly reproduced in the shape of the measured γ -ray peaks. In reality, $\sigma(E)$ varies significantly with the beam energy over the thickness of the target and the calculated peak shape was

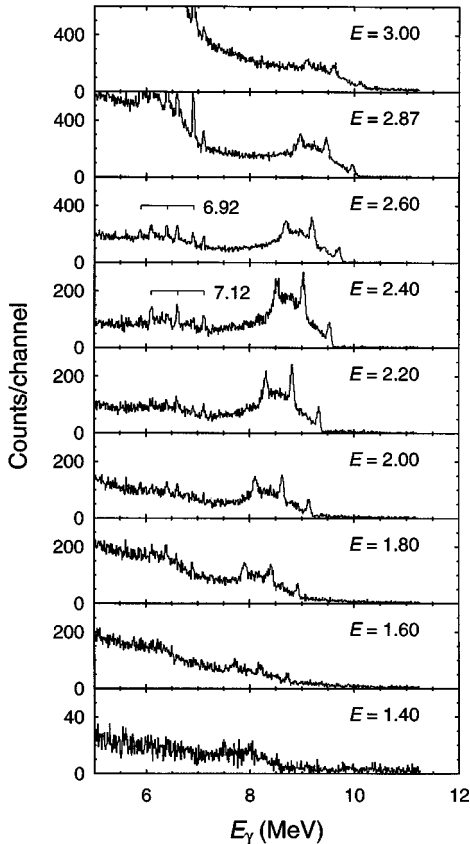


FIG. 8. Sample γ -ray spectra at 90° in the region of interest, for each of the nine center-of-mass energies studied in the present work. One can note the shift of the three peaks of the ground state transition with $E_{\text{c.m.}}$. Also indicated are the fixed lines from the cascade through the 6.917- and 7.117-MeV levels, which are stronger at higher beam energy.

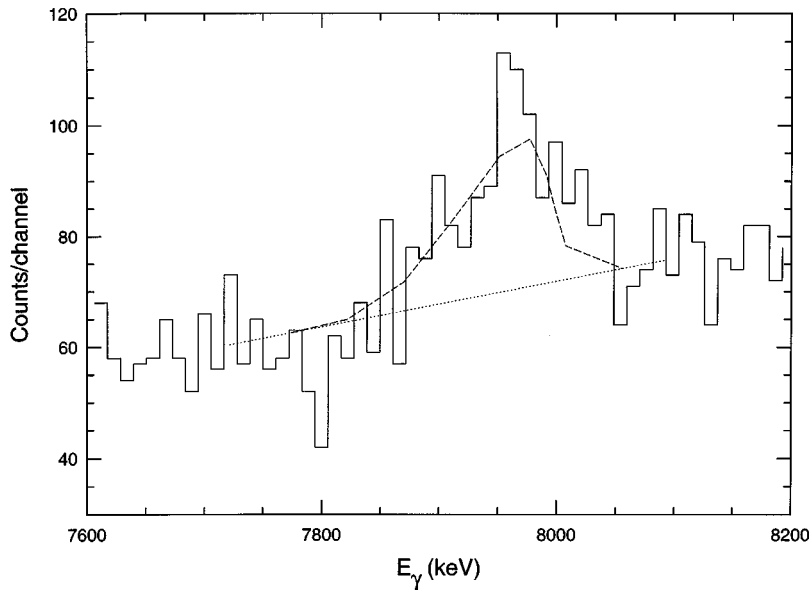


FIG. 9. Sample result of the fit of a γ -ray peak. The histogram is the spectrum data, and the dotted line represents the straight background deduced from counts in a few channels on either side of the peak. The dashed line is the shape computed from the results of the narrow resonance scans, after its area and position had been fitted to the peak.

corrected for that. Since the position on the energy scale of the centroid was affected by this correction, the procedure was iterated three times. Finally, the finite resolution of the system was included by a convolution of the expected shape with a Gaussian of 30 keV FWHM to account for the Doppler broadening.

C. Calculation of $E1$ and $E2$ cross sections

For each experimental run, six spectra were accumulated. A linear background was assumed under the full-energy, single-escape, and double-escape peaks of the γ rays of $^{12}\text{C}(\alpha, \gamma)^{16}\text{O}$, and areas were obtained as follows. The expected peak profile was fitted to all the observed γ -ray peaks with a simple chi-squared minimization method (Fig. 9). The free parameters were the area under the peak (in number of counts) and the position of the shape centroid. Initial values were obtained from a direct centroid calculation on the spectrum peaks. The minimum reduced χ^2 was seldom larger than 1, and the parameters after the fit usually differed from the initial values by an amount smaller than the uncertainties. The areas and energies obtained from the fit were used in the rest of the analysis; they were assigned the errors predicted by the direct centroid calculation. These areas were divided by the relative efficiency of the appropriate Ge detector to yield eighteen numbers proportional to differential cross sections. The weighted averages of the three values produced by each detector (one for each peak) were taken. The resulting six values (covering five angles) were fitted using the angular distribution function given by

$$\begin{aligned}
 W(\theta) = & 1 - Q_2 P_2(\theta) + (\sigma_{E2}/\sigma_{E1}) \\
 & \times [1 + \frac{5}{7} Q_2 P_2(\theta) - \frac{12}{7} Q_4 P_4(\theta)] \\
 & + \frac{6}{5} \sqrt{5} (\sigma_{E2}/\sigma_{E1})^{1/2} \cos\Phi [Q_1 P_1(\theta) - Q_3 P_3(\theta)],
 \end{aligned}
 \tag{2}$$

where $P_l(\theta)$ is the Legendre polynomial of order l and Q_l is the corresponding attenuation factor (to be given the appropriate value for each detector; see Table I). During those fits,

the following parameters were varied: an overall amplitude (proportional to σ_{E1}) multiplying $W(\theta)$, the square root of σ_{E2}/σ_{E1} , and the phase angle Φ . The parameters for all 16 runs are presented in Table II, and Fig. 10 gives the normalized yields and the best fit for the nine sample angular distributions shown (one at each energy studied). The errors in the parameters correspond to an increase of 1 of the total χ^2 above its minimum [16]. The $E2$ contribution to the reaction was obtained from the $E1$ contribution and the σ_{E2}/σ_{E1} ratio, taking into account their correlation when determining the uncertainty.

The $E1$ and $E2$ contributions were divided by the target thickness (in ^{12}C atoms/cm²) and the total charge deposited on the target (in number of ^4He ions). (In the analysis of Ref. [9], the target thicknesses were erroneously expressed in energy units.) The results were normalized by requiring that the total cross section at $E=2.4$ MeV from the present work be equal to the accepted value at the maximum of the wide $J^\pi=1^-$ resonance. The cross section used for reference, $\sigma=47\pm 3$ nb, is the weighted average of the results of previous work as suggested by Ref. [4]. The normalization factor came to 1.67×10^{-7} . For comparison, the factor deduced from the absolute calibration of the detectors would be 2.25×10^{-7} with the value of Ref. [14] for the width of the 992 keV resonance of $^{27}\text{Al}(p, \gamma)^{28}\text{Si}$ (24.2 eV). For reference, Table III lists the absolute differential cross sections that are obtained when the normalization of the integrated cross sections is applied to the differential values. The energy attributed to each run was determined from the centroids of the γ -ray peaks in the two detectors at 90° and the Q value of the reaction, 7162 keV [17]. The weighted average of the six values (from the full energy, single escape and double escape peaks) was typically 20–30 keV below the center-of-mass energy deduced from the incident beam energy and slightly higher than the value at half the target thickness.

The final $E1$ and $E2$ cross sections and the S factors, averaged over experimental runs when necessary, are given in Table IV. The errors quoted in this table do not include the 6% uncertainty from the overall normalization. When there

TABLE II. Results of all individual runs from the present work.

$E_{\text{c.m.}}$		Target							
Nom. (MeV)	Effect. (keV)	No.	t_C (keV)	n_C (10^{18} cm^{-2})	Q (C)	σ_{E1} (nb)	σ_{E2}/σ_{E1}	Φ ($^\circ$)	σ_{E2}^a (nb)
2.40	2382.6 \pm 2.1	1	66.0	4.64	1.08	50.6 \pm 2.6	0.049 \pm 0.038	b	2.5 \pm 1.9
2.20	2172.0 \pm 2.4	1	61.3	4.06	2.34	20.5 \pm 1.2	0.044 \pm 0.044	b	0.90 \pm 0.88
2.00	1979.0 \pm 2.8	1	57.0	3.54	5.76	6.87 \pm 0.43	0.032 \pm 0.053	b	0.22 \pm 0.36
2.87	2834.9 \pm 2.0	2	69.6	5.50	6.12	6.40 \pm 0.37	0.32 \pm 0.07	85 \pm 3	2.06 \pm 0.36
2.60	2570.5 \pm 2.0	2	67.9	5.04	2.40	25.0 \pm 1.2	0.119 \pm 0.039	64 \pm 4	3.0 \pm 0.9
3.00	2981.5 \pm 3.8	2	51.2	4.16	7.29	3.18 \pm 0.36	1.09 \pm 0.23	105 \pm 4	3.45 \pm 0.44
3.00	2984.9 \pm 7.3	2	42.6	3.46	4.32	2.8 \pm 0.6	1.79 \pm 0.55	88 \pm 6	5.0 \pm 0.7
1.80	1777.1 \pm 3.2	3	77.4	4.46	11.55	2.18 \pm 0.17	0.20 \pm 0.08	53 \pm 8	0.42 \pm 0.16
1.60	1579.3 \pm 6.3	5	57.6	3.07	16.86	1.02 \pm 0.12	0.21 \pm 0.15	54 \pm 15	0.21 \pm 0.14
1.60	1576.0 \pm 7.6	6	59.5	3.18	8.64	0.84 \pm 0.15	0.52 \pm 0.27	58 \pm 12	0.44 \pm 0.17
1.60	1577.4 \pm 11.2	6	41.9	2.24	5.76	0.45 \pm 0.19	1.49 \pm 1.06	80 \pm 14	0.67 \pm 0.25
1.40	1361.8 \pm 10.3	8	52.0	2.55	10.32	0.32 \pm 0.09	0.74 \pm 0.53	64 \pm 15	0.24 \pm 0.12
2.40	2389.6 \pm 1.3	9	51.4	3.61	5.28	42.4 \pm 2.0	0.030 \pm 0.036	b	1.3 \pm 1.5
2.60	2589.9 \pm 1.5	9	35.2	2.61	11.04	22.1 \pm 1.0	0.136 \pm 0.039	76 \pm 3	3.0 \pm 0.8
1.40	1382.1 \pm 12.1	10	57.2	2.81	11.56	0.23 \pm 0.08	0.88 \pm 0.70	79 \pm 16	0.20 \pm 0.11
1.40	1370.2 \pm 11.2	11	47.2	2.32	7.80	0.38 \pm 0.12	0.34 \pm 0.50	80 \pm 23	0.13 \pm 0.16

^aThe errors take into account the anticorrelation between S_{E1} and σ_{E2}/σ_{E1} .

^bNot determined from the data.

is more than one run at a given energy, the $E2$ cross section is the weighted average of the individual $E2$ cross sections.

IV. ANALYSIS AND EXTRAPOLATION

A. K -matrix fit of $E1$ contribution

In order to study the implications of the measurement made here, a global K -matrix fit [18,19] was made for the full $^{12}\text{C}(\alpha, \gamma)^{16}\text{O}$ data set (this work, plus Refs. [4,6,8]), along with the phase shifts from elastic scattering [5] and the β -delayed α spectrum from the decay of ^{16}N [10]. We employ similar notation to that found in Ref. [10].

The following fitting functions were used.

The $E1$ part of the $^{12}\text{C}(\alpha, \gamma)$ cross section:

$$\sigma_{E1}(E) = \frac{12\pi}{k_\alpha^2} p_{1\alpha}^2 p_{1\gamma}^2 \frac{|K_{1\alpha\gamma}|^2}{1 + p_{1\alpha}^4 p_{1\alpha}^2}. \quad (3)$$

The elastic scattering phase shift:

$$\delta_l(E) = \tan^{-1}(p_{l\alpha}^2 K_{l\alpha\alpha}). \quad (4)$$

The α spectrum from the ^{16}N decay:

$$W_\alpha(E) = f_\beta(E) \sum_{l=1,3} p_{l\alpha}^2 \frac{|K_{l\beta\alpha}|^2}{1 + p_{l\alpha}^4 K_{l\alpha\alpha}^2}, \quad (5)$$

where $f_\beta(E)$ is the integrated Fermi function. In performing the fit, this spectrum was convolved with a Gaussian resolution function of FWHM 30 keV, as specified in Ref. [10].

The K -matrix element for multipole l , connecting channels i and j , is parametrized as

$$K_{lij} = \sum_{\lambda=1}^2 \frac{g_{li\lambda} g_{lj\lambda}}{E_{l\lambda} - E} + D_{lij}. \quad (6)$$

For the radiative capture channel, $g_{li\lambda}$ is the reduced width amplitude for level λ . For the β -decay channel, $g_{li\lambda}$ equals the $B_{l\lambda}$ and p_{li} is the K -matrix penetrability for channel i . The background terms, D_{lij} , are energy dependent and were taken to be of the form

$$D_{lij} = -\frac{g_{li3} g_{lj3}}{E_{l3} - E} + b_{lij}, \quad (7)$$

with b_{lij} constant. The sign convention chosen corresponds to an echo pole in the background.

In order to get a reliable estimate on the uncertainties in $S_{E1}(300)$ for a given fit, we made the standard replacement for $g_{1\alpha 1}$, using the relation

$$g_{1\alpha 1} = \left(\frac{E_{11} - 0.3}{g_{1\gamma 1}} \right) \left[\frac{S_{E1}(300)^{1/2}}{1.2472} - \frac{g_{1\alpha 2} g_{1\gamma 2}}{E_{12} - 0.3} - D_{1\alpha\gamma}(0.3) \right]. \quad (8)$$

The fitting was done with the CERN package MINUIT [20]. In using the elastic scattering data [5], we followed the practice of omitting the $l=1$ phase shifts for $E_\alpha > 5.05$ MeV, due to concerns about the fluctuating energy dependence in this range. When using the ^{16}N results [10], we followed the suggestion of those authors and removed the data for energies between 2.64 and 2.75 MeV. The uncertainties in the values of $S_{E1}(300)$ represent a change in χ^2 of 5%, following the treatment of Ref. [19].

We first looked at the minimal fit that can be sensibly performed, using the present results and the elastic scattering data of Plaga *et al.* [5]. The energy and reduced γ width of the subthreshold state were fixed, as was the position of the background echo pole (at 100 MeV), corresponding to the choice of Ref. [10]. In this fit, the subthreshold α width was unconstrained, and it is clear from Fig. 11(a) and fit 1 of

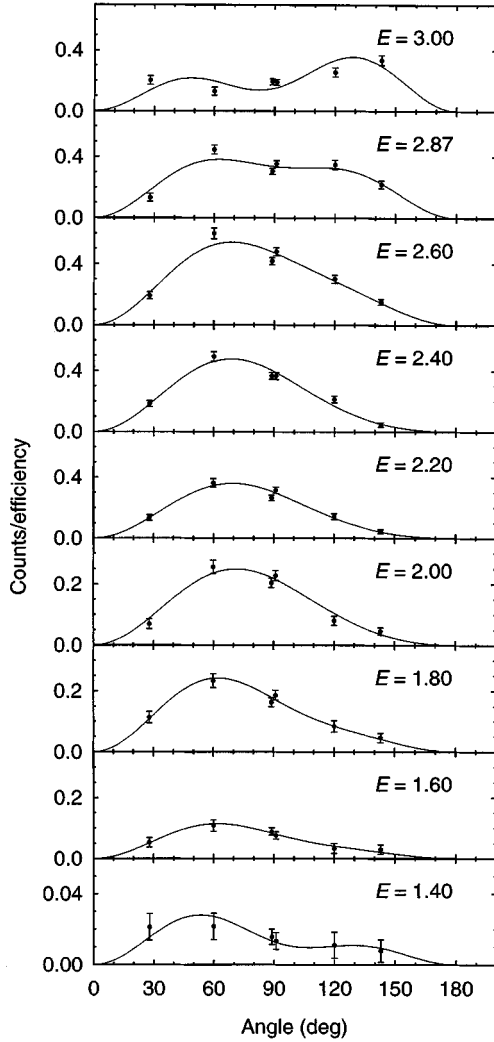


FIG. 10. Angular distributions at the nine energies covered by the present study. For clarity, the points due to the two detectors at 90° are shown slightly offset from that angle. The general shape of most distributions corresponds to a dominant $E1$ transition with a small $E2$ admixture. The effect of the finite detector size has been removed from the fit (see text).

Table V that the data prefer a small width and, thus, a relatively small value of $S_{E1}(300)$ of 65.7 ± 16.5 keV b.

Extending the fit to include the ^{16}N numbers imposed a severe constraint on the subthreshold width. This led to an increase in the extrapolated value of $S_{E1}(300)$ to 83.4 ± 4.9 keV b, as seen in Fig. 11(a) and fit 2 of Table V. For this fit, some additional parameters were fixed according to the prescriptions of Ref. [10], particularly those for some of the $l=3$ states. It can easily be seen from the χ^2 for the (α, γ) channel for fit 2 of Table V that the fit reproduces the data extremely well.

Finally, a full fit [Fig. 11(b)] including all other radiative capture results [4,6,8] yielded an extrapolated value of $S_{E1}(300)$ equal to 84.8 ± 3.9 keV b. The change in S is small compared to fit 2, and there is little change in any of the significant factors.

In a similar manner to Ref. [10], we can investigate the spread in $S_{E1}(300)$ through the systematic differences in each (α, γ) data set, fitted separately. The uncertainty inferred

from this would be larger than that from the global fit and would imply a value of $S_{E1}(300) = 84.8 \pm 15.7$ keV b.

A search was also done in each of the three cases presented above for a fit that showed destructive interference between the subthreshold state and the 2.4-MeV resonance in the $^{12}\text{C}(\alpha, \gamma)^{16}\text{O}$ cross section and a corresponding low value for $S_{E1}(300)$. The minimum χ^2 for each case was significantly larger than that found for constructive interference, and thus destructive interference would appear to be ruled out.

B. R -matrix fit of the $E1$ contribution

We have also made a global R -matrix fit of the same data set as considered in the K -matrix fit. Again, we employ similar notation to that found in Ref. [10].

We fit the following functions to the data set.

The $E1$ part of the $^{12}\text{C}(\alpha, \gamma)$ cross section:

$$\sigma_{E1}(E) = \frac{6\pi}{k_\alpha^2} P_1 \frac{|R_{1\alpha\gamma}|^2}{[1 - (S_1 - B_1)R_{1\alpha\alpha}]^2 + P_1^2 R_{1\alpha\alpha}^2}, \quad (9)$$

where P_l is the penetrability, S_l is the shift function (both calculated at E and the channel radius a [21]), and B_l is the boundary parameter.

The elastic scattering phase shift:

$$\delta_l(E) = -\Phi_l + \tan^{-1} \left(\frac{P_l}{R_{l\alpha\alpha}^{-1} - S_l + B_l} \right), \quad (10)$$

where Φ_l is the hard-sphere phase shift.

The α spectrum from the ^{16}N decay:

$$W_\alpha(E) = f_\beta(E) \sum_{l=1,3} P_l \frac{|R_{l\beta\alpha}|^2}{[1 - (S_l - B_l)R_{l\alpha\alpha}]^2 + P_l^2 R_{l\alpha\alpha}^2}. \quad (11)$$

In performing the fit, this spectrum is convolved with a Gaussian resolution function of FWHM 30 keV, as specified in Ref. [10]:

The elements of the R matrix are parametrized as

$$R_{l\alpha\alpha} = \sum_{\lambda=1}^3 \frac{\gamma_{l\lambda}^2}{E_{l\lambda} - E}, \quad (12)$$

$$R_{1\alpha\gamma} = \sum_{\lambda=1}^3 \frac{\gamma_{1\lambda} \Gamma_{\gamma\lambda}^{1/2}}{E_{1\lambda} - E}, \quad (13)$$

$$R_{l\beta\alpha} = \sum_{\lambda=1}^3 \frac{A_{l\lambda}}{E_{l\lambda} - E}. \quad (14)$$

$\gamma_{l\lambda}$ represent the reduced alpha width amplitudes, $A_{l\lambda}$ are the β -feeding amplitudes, and $\Gamma_{\gamma\lambda}$ is the full γ width of each state.

It is well known that the choice of B_l cannot affect the fit [22]. Through using $B_l = S_l(E_{l1})$, we can use the experimentally determined values of $\Gamma_{\gamma l}$, and the beta-decay branching ratios for the $l=1$ and $l=3$ subthreshold states, through the relations

TABLE III. $^{12}\text{C}(\alpha,\gamma)^{16}\text{O}$ differential cross sections.

E_{nom} (MeV)	$E_{\text{c.m.}}$ (keV)	28° (nb)	60° (nb)	90° (nb)	90° (nb)	120° (nb)	143° (nb)
2.40	2382.6±2.1	2.78±0.32	7.52±0.47	5.58±0.33	5.56±0.34	3.23±0.33	0.72±0.22
2.00	1979±2.8	0.26±0.06	0.96±0.08	0.76±0.06	0.86±0.06	0.30±0.06	0.17±0.05
2.20	2172±2.4	1.08±0.15	2.92±0.23	2.12±0.15	2.54±0.16	1.15±0.16	0.36±0.10
2.60	2570±2.0	1.22±0.14	3.79±0.23	2.64±0.15	3.03±0.16	1.91±0.17	0.96±0.12
2.87	2834.9±2.0	0.30±0.06	1.01±0.07	0.69±0.05	0.80±0.05	0.79±0.07	0.50±0.06
3.00	2981.5±3.8	0.51±0.07	0.33±0.07	0.48±0.05	0.48±0.05	0.64±0.07	0.85±0.08
3.00	2984.9±7.3	0.54±0.13	0.85±0.12	0.34±0.08	0.50±0.08	0.81±0.13	0.74±0.13
1.80	1777.1±3.2	0.17±0.03	0.35±0.03	0.24±0.02	0.28±0.02	0.13±0.03	0.07±0.02
1.60	1579.3±6.3	0.08±0.02	0.16±0.03	0.13±0.02	0.11±0.02	0.05±0.02	0.04±0.02
1.60	1576.0±7.6	0.07±0.03	0.21±0.03	0.11±0.02	0.10±0.02	0.04±0.03	0.08±0.03
1.60	1577.4±11.2	0.08±0.04	0.14±0.04	0.08±0.03	0.05±0.03	0.11±0.04	0.07±0.05
1.40	1361.8±10.3	0.06±0.02	0.06±0.02	0.05±0.01	0.04±0.01	0.03±0.02	0.02±0.02
2.40	2389.6±1.3	1.91±0.24	5.43±0.30	4.71±0.23	5.00±0.24	2.39±0.24	1.24±0.22
2.60	2589.9±1.5	1.15±0.13	2.67±0.16	2.48±0.12	2.67±0.13	1.92±0.14	1.09±0.11
1.40	1382.1±12.1	0.03±0.02	0.05±0.02	0.03±0.01	0.04±0.01	0.03±0.02	0.04±0.02
1.40	1370.2±11.2	0.03±0.03	0.05±0.03	0.04±0.02	0.05±0.02	0.03±0.03	0.04±0.03

$$\Gamma_{\gamma 1} = \Gamma_{\gamma 1}^{\text{obs}} \left(1 + \gamma_{11}^2 \frac{dS_1}{dE}(E_{11}) \right), \quad (15)$$

$$A_{11}^2 = \frac{N_a Y_{11}}{Y(9.59) I_{11} f_{11}}, \quad (16)$$

$$I_{11} = \pi \gamma_{11}^{-2} \left(1 + \gamma_{11}^2 \frac{dS_1}{dE}(E_{11}) \right)^{-1}, \quad (17)$$

where $Y_{11}/Y(9.59)$ represents the branching ratio of each subthreshold state relative to the state at $E=9.59$ MeV.

We first consider a fit of this data set, along with the elastic scattering data of Plaga *et al.* [5] and the ^{16}N data of Azuma *et al.* [10]. As mentioned, the boundary condition $B_l = S_l(E_{11})$ is imposed and a channel radius of $a=6.5$ fm is used, in line with the best fit of Ref. [10]. We see from fit 1 of Table VI that the best fit here yields a value of $S_{E1}(300)=77.8\pm 5.3$ keV b. A global fit, including the $^{12}\text{C}(\alpha,\gamma)$ data of Refs. [6,4,8], is also performed and shown

in fit 2 of Table VI. This yields a value for $S_{E1}(300)=73.3\pm 4.2$ keV b. The two fits are shown in Figs. 12(a) and 12(b), respectively.

If we include the effects of varying a over acceptable values, then this contribution to the uncertainty yields $S_{E1}(300)=73.3\pm 13.2$ keV b.

C. $E2$ contribution

The electric quadrupole contribution for each experimental run was obtained directly from the data, by the multiplication of the $E1$ component and the σ_{E2}/σ_{E1} ratio produced by the fit. Normalization and averaging yielded the final values listed in Table IV. The procedure used for their extrapolation is based on the formalism developed by Langanke and Koonin [23]. As opposed to the $E1$ situation, a more microscopic approach is useful here because of the relatively smooth behavior of the $E2$ cross section at low energy. There is only one resonance, at subthreshold, contributing to the S factor in a significant way.

The $E2$ cross section can be written as

TABLE IV. Average $E1$ and $E2$ cross sections and S factors.

E_{nom} (MeV)	$E_{\text{c.m.}}$ (keV)	σ_{E1} (nb)	S_{E1} (keV b)	σ_{E2}^a (nb)	S_{E2} (keV b)
1.40	1370.3±6.4	0.29±0.06	17.1±3.2	0.20±0.07	11.7±4.1
1.60	1577.9±4.5	0.85±0.09	17.3±1.8	0.36±0.10	7.3±2.0
1.80	1777.1±3.2	2.18±0.17	19.5±1.5	0.42±0.16	3.8±1.4
2.00	1979.0±2.8	6.87±0.43	30.5±1.9	0.22±0.36	1.0±1.6
2.20	2172.0±2.4	20.5±1.2	51.3±2.9	0.90±0.88	2.3±2.2
2.40	2387.7±1.1	45.2±1.8	65.6±2.6	1.8±1.2	2.6±1.7
2.60	2583.1±1.2	23.2±0.9	21.9±0.9	3.0±0.6	2.8±0.6
2.87	2834.8±2.0	6.4±0.4	3.67±0.21	2.06±0.36	1.18±0.21
3.00	2982.2±3.4	3.1±0.3	1.36±0.14	3.87±0.38	1.72±0.17

^aCalculated from the average of the $E2$ cross sections of individual runs.

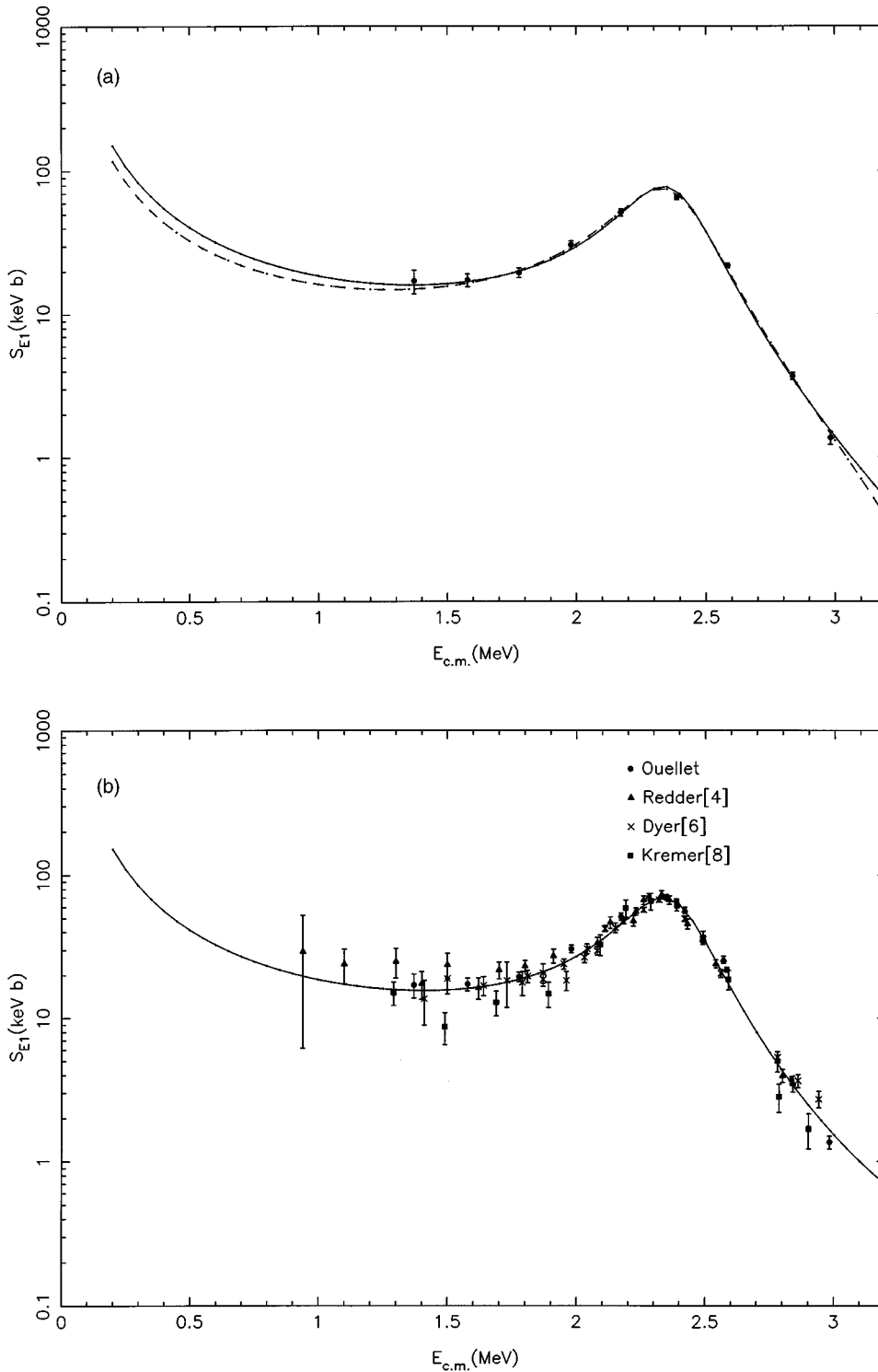


FIG. 11. (a) The $E1$ astrophysical S factors from the present experiment. The dashed line indicates the K -matrix fit to the present $E1$ data and the elastic scattering data of Plaga *et al.* [5]. The fit parameters appear in Table V, fit 1. The solid line represents the K -matrix fit obtained when the ^{16}N data of Azuma *et al.* [10] is included. The fit parameters are given in Table V, fit 2. (b) The $E1$ astrophysical S factors from the present experiment and Refs. [4,6,8]. The solid line represents a K -matrix fit to the data from these measurements, the elastic scattering data of Plaga *et al.* [5], and the ^{16}N data of Azuma *et al.* [10]. The fit parameters are given in Table V, fit 3.

$$\sigma_{E2} = \frac{4\pi}{375} \left(\frac{E}{\hbar c} \right)^5 \frac{1}{\hbar v_{\text{rel}}} |\langle \psi_{l=2}^i(E_{\text{c.m.}}) | Q_2 | \psi_{l=0}^f \rangle|^2, \quad (18)$$

where $E = E_{\text{c.m.}} + 7.162$ MeV and Q_2 is the electromagnetic quadrupole operator. In the reaction of interest, ψ^i is the continuum $\alpha + ^{12}\text{C}$ wave function and ψ^f is the ^{16}O ground state.

We can expand Q_2 as

$$Q_2 = Q_{2\alpha} + Q_{2C} + Q_{2r}. \quad (19)$$

Q_{2r} acts on the relative coordinate between the α particle and the ^{12}O nucleus, while the other two terms are intrinsic to each particle.

The continuum and bound-state wave functions are described in the cluster model [24,25]. In a harmonic oscillator basis they appear as

$$\psi_{l=2}^i = \sum_n \frac{1}{\sqrt{N_{n,l=2}}} \langle u_{n,l} | g_{l=2} \rangle \mathcal{A} \{ \phi_\alpha \phi_C^{l=0} u_{n,l=2} \} \quad (20)$$

TABLE V. Best fit parameters from K -matrix analyses of $E1$ cross sections. Fit 1 is the present data and the elastic scattering phase shifts from Ref. [5]; fit 2 adds the ^{16}N data of Ref. [10]; fit 3 includes all data of fits 1 and 2, plus the (α, γ) cross sections of Refs. [6], [4], [8]. The β -feeding amplitudes B_{ij} are shown scaled by the total number of counts $N_\alpha = 1.0265 \times 10^6$. The uncertainties given for S reflect those from the specific fit only.

Parameter		Fit 1	Fit 2	Fit 3
$g_{1\alpha 1} a^{-3/2}$ (MeV $^{1/2}$)	from Eq. (8)	-6.214	-7.134	-7.112
$g_{1\alpha 2} a^{-3/2}$ (MeV $^{1/2}$)		7.140	6.913	6.914
$g_{1\alpha 3} a^{-3/2}$ (MeV $^{1/2}$)		-387.4	-340.1	-340.6
$g_{3\alpha 1} a^{-7/2}$ (MeV $^{1/2}$)			6.145×10^{-2}	6.150×10^{-2}
$g_{3\alpha 2} a^{-7/2}$ (MeV $^{1/2}$)			6.399×10^{-2}	6.399×10^{-2}
$g_{3\alpha 3} a^{-7/2}$ (MeV $^{1/2}$)			-0.448	-0.448
$g_{1\gamma 1} a^{-3/2}$ (MeV $^{1/2}$)	fixed	1.897×10^{-3}	1.897×10^{-3}	1.897×10^{-3}
$g_{1\gamma 2} a^{-3/2}$ (MeV $^{1/2}$)		7.085×10^{-4}	6.957×10^{-4}	6.598×10^{-4}
$g_{1\gamma 3} a^{-3/2}$ (MeV $^{1/2}$)		-1.587×10^{-2}	-1.337×10^{-2}	-2.654×10^{-2}
$B_{11} / \sqrt{N_\alpha}$	fixed		1.21	1.21
$B_{12} / \sqrt{N_\alpha}$			-0.4233	-0.4233
$B_{13} / \sqrt{N_\alpha}$			21.56	21.23
$B_{31} / \sqrt{N_\alpha}$	fixed		2.5	2.5
$B_{32} / \sqrt{N_\alpha}$	fixed		0	0
$B_{33} / \sqrt{N_\alpha}$	fixed		0	0
E_{11} (MeV)	fixed	-0.0451	-0.0451	-0.0451
E_{12} (MeV)		2.455	2.451	2.451
E_{13} (MeV)	fixed	100	100	100
E_{31} (MeV)	fixed		-1.032	-1.032
E_{32} (MeV)			4.414	4.414
E_{33} (MeV)	fixed		15	15
$b_{1\alpha\alpha} a^{-3}$		1588.7	1232.0	1235.4
$b_{3\alpha\alpha} a^{-7}$			2.267×10^{-2}	2.268×10^{-2}
$b_{1\gamma\alpha} a^{-3}$		0.723×10^{-2}	4.656×10^{-2}	9.223×10^{-2}
$b_{1\beta\alpha} a^{-3/2} \sqrt{N_\alpha}$ (MeV $^{-1/2}$)			-77.50	-76.44
$b_{3\beta\alpha} a^{-7/2} \sqrt{N_\alpha}$ (MeV $^{-1/2}$)	fixed		0	0
$S(0.3 \text{ MeV})$ (keV b)		65.7 ± 16.0	83.4 ± 4.9	84.8 ± 3.9
$\chi^2(\alpha, \gamma)$		($N=9$) 5.94	($N=9$) 14.8	($N=71$) 156.2
$\chi^2(\alpha, \alpha) l=1$		($N=26$) 27.16	($N=26$) 33.4	($N=26$) 33.3
$\chi^2(\alpha, \alpha) l=3$			($N=40$) 57.0	($N=40$) 57.0
$\chi^2 \text{ } ^{16}\text{N}$			($N=87$) 98.1	($N=87$) 98.3

and

$$\psi_{l=0}^i = \sum_n \frac{1}{\sqrt{N_{n,l=0}}} \langle u_{n,l} | g_{l=0} \rangle \mathcal{A} \{ \phi_\alpha \phi_C^{l=0} u_{n,l=0} \}. \quad (21)$$

\mathcal{A} ensures the antisymmetry of the 16-particle states, and $N_{n,l}$ is a normalization constant. The functions $u_{n,l}$ are harmonic oscillator wave functions in the relative coordinate, while $g_l(r)$ represents the solution of the wave equation in the relative coordinate:

$$\Lambda \left(\frac{-\hbar^2}{2\mu} \frac{\partial^2}{\partial r^2} + V(r) - \frac{l(l+1)\hbar^2}{2\mu r^2} - E \right) g_l(r) = 0. \quad (22)$$

The operator Λ ensures that the Pauli principle is obeyed and that the wave function is correctly damped in the internal region. We use

$$\Lambda = 1 - |u_{0,l}\rangle \langle u_{0,l}| - |u_{1,l}\rangle \langle u_{1,l}| \quad (23)$$

for the $E2$ case.

$V(r)$ is the potential that describes the relative interaction, and it is taken here to be a Gaussian of the form

$$V(r) = V_0 e^{-r^2/r_0^2}. \quad (24)$$

For the ^{16}O ground state, the parameters are chosen to fit the binding energy relative to the $\alpha + ^{12}\text{C}$ threshold. $r_0 = 2.3$ fm was fixed in this fit, as in Ref. [23]. The difference is in the treatment of excited states. Reference [23] chose to constrain the parameters from 2^+ states by fitting known levels and transition rates separately. The $E2$ capture rate was then, effectively, a prediction of the model. Instead, we follow the procedure of Zhao *et al.* [26], who chose to fix $r_0 = 2.8$ fm in the continuum state and treat V_0 as a free parameter in the least-squares fit to the $E2$ cross section. This approach is more phenomenological and better allows the data to drive the extrapolation of the $E2$ cross section to 300 keV, the energy of interest.

TABLE VI. A global R -matrix fit of our measured $E1$ cross section. Fit 1 is for the same data set as fit 2 from Table V; fit 2 is for the same data set as fit 3. The β -feeding amplitudes $A_{I\lambda}$ are shown scaled by the total number of counts $N_\alpha=1.0265\times 10^6$. The channel radius for the fit was $a=6.5$ fm. The uncertainties quoted for S are from the specific fit only.

Parameter		Fit 1	Fit 2
γ_{11} (MeV ^{1/2})		0.0667	0.0662
γ_{12} (MeV ^{1/2})		0.3206	0.3206
γ_{13} (MeV ^{1/2})		2.653	2.861
γ_{31} (MeV ^{1/2})		0.0734	0.0734
γ_{32} (MeV ^{1/2})		0.2506	0.2505
γ_{33} (MeV ^{1/2})		1.292	1.289
$\gamma_{\gamma 1}$ (MeV ⁻¹)	from Eq. (15)	9.149×10^{-6}	9.141×10^{-6}
$\gamma_{\gamma 2}$ (MeV ⁻¹)		-2.403×10^{-6}	-2.350×10^{-6}
$\gamma_{\gamma 3}$ (MeV ⁻¹)		-1.052×10^{-5}	-9.887×10^{-6}
$A_{11}/\sqrt{N_\alpha}$ (MeV ^{1/2})	from Eq. (16)	0.0848	0.0838
$A_{12}/\sqrt{N_\alpha}$ (MeV ^{1/2})		0.1777	0.1777
$A_{13}/\sqrt{N_\alpha}$ (MeV ^{1/2})		-4.038	-4.715
$A_{31}/\sqrt{N_\alpha}$ (MeV ^{1/2})	from Eq. (16)	0.1852	0.1854
$A_{32}/\sqrt{N_\alpha}$ (MeV ^{1/2})	fixed	0	0
$A_{33}/\sqrt{N_\alpha}$ (MeV ^{1/2})	fixed	0	0
E_{11} (MeV)	fixed	-0.0451	-0.0451
E_{12} (MeV)		2.836	2.836
E_{13} (MeV)	fixed	62.94	72.73
E_{31} (MeV)	fixed	-1.032	-1.032
E_{32} (MeV)		4.793	4.792
E_{33} (MeV)	fixed	18.99	18.91
$S(0.3$ MeV) (keV b)		77.8 ± 5.4	73.3 ± 4.2
$\chi^2(\alpha, \gamma)$		($N=9$) 13.0	($N=71$) 155.0
$\chi^2(\alpha, \alpha) L=1$		($N=26$) 33.2	($N=26$) 33.2
$\chi^2(\alpha, \alpha) L=3$		($N=40$) 59.7	($N=40$) 59.7
χ^2 ¹⁶ N		($N=87$) 112.4	($N=87$) 112.7

In order to obtain the correct binding energy and lifetime for the subthreshold 2^+ level, the depth of the potential would have to be $V_0=-103.5$ MeV. However, the present, rather small $E2$ cross sections force that parameter to a different value due to a larger contribution from the subthreshold 2^+ level. The fit yielded $V_0=-110.3\pm 0.3$ MeV, a reduced χ^2 of 1.8, and $S_{E2}(300)=36\pm 6$ keV b. The small extrapolated uncertainty is a consequence of the fact that the model used only one free parameter (V_0) and the fit is driven by the most precisely determined point at high energy. Figure 13(a) shows the data, the line of best fit, and the extrapolated S_{E2} . The present $E2$ cross sections are in good agreement with those of Redder *et al.* [4] [Fig. 13(b)]. Both these data sets give values systematically smaller than those of Kettner *et al.* [7], especially at low energy.

V. CONCLUSIONS

The discrepancy between published values of the $^{12}\text{C}(\alpha, \gamma)^{16}\text{O}$ $E1$ cross section at low energies has been a major problem in many attempts to deduce a reliable extrapolation of the value of the $E1$ capture S factor at 300 keV, $S_{E1}(300)$, for this important reaction. This is due to the fact that the influence of the α width of the 1^- subthreshold state on the radiative capture and the elastic scattering cross section above 1 MeV is very weak. Measurements [10,27] of

the delayed α spectrum following the β decay of ^{16}N provide a reliable value of this α width. However, they cannot measure the relative phases of the radiative capture amplitudes from the different 1^- levels. It takes a combination of all three measurements, radiative capture, elastic scattering, and delayed α -emission measurements, to yield a reliable value of $S_{E1}(300)$.

Least-squares fits to the present data, the elastic scattering data of Plaga *et al.* [5], and the ^{16}N data of Azuma *et al.* [10] give a value of $S_{E1}(300)=83.4\pm 4.9$ keV b using the K -matrix formalism and $S_{E1}(300)=77.8\pm 5.3$ keV b using the R -matrix formalism.

As discussed earlier, the different values of $S_{E1}(300)$ deduced from different sets of radiative capture data are not in agreement. As explained in Sec. IV A it would therefore seem appropriate to increase the uncertainty to account for this discrepancy. The result of the K -matrix least-squares fitting to all radiative capture data, elastic scattering data, and ^{16}N decay data then gives $S_{E1}(300)=85\pm 15$ keV b and the R matrix gives 73 ± 13 keV b. Both extrapolations are in reasonable agreement with the analysis published by Azuma *et al.* [10]. The ratio of the reduced alpha widths of the 1^- levels at 7.1 and 9.6 MeV deduced from these latest measurements is $\theta^2(7.1)/\theta^2(9.6)=0.035$. This is a factor of 10 smaller than the ratio obtained from stripping reactions [28].

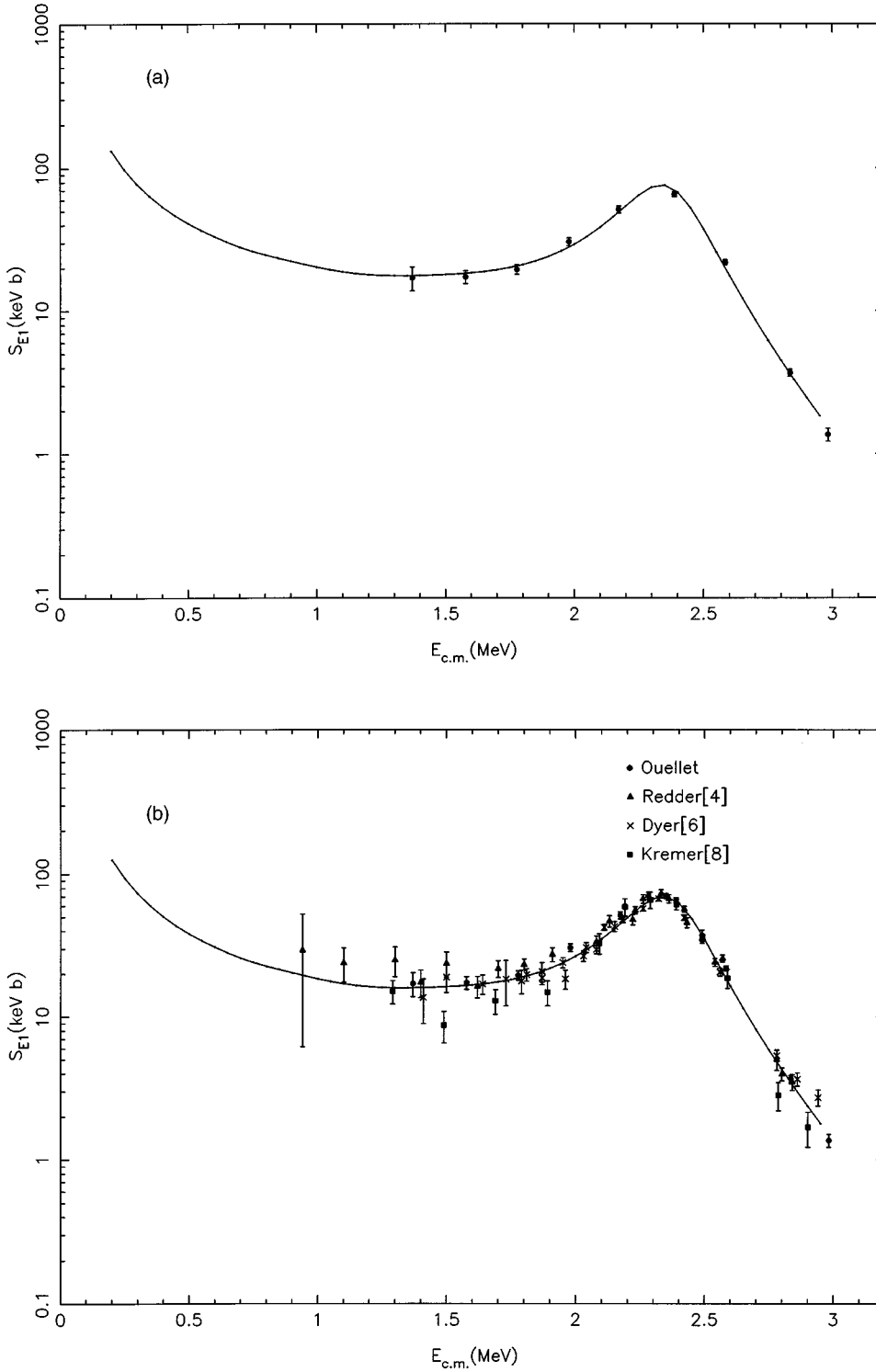


FIG. 12. (a) The $E1$ astrophysical S factors from the present experiment. The solid line represents an R -matrix fit to the present data, the elastic scattering data of Plaga *et al.* [5], and the ^{16}N data of Azuma *et al.* [10]. The fit parameters are given in Table VI, fit 1. (b) The $E1$ astrophysical S factors from the present experiment and Refs. [4,6,8]. The R -matrix fit includes these data, the elastic scattering data of Plaga *et al.* [5], and the ^{16}N data of Azuma *et al.* [10]. The fit parameters are given in Table VI, fit 2.

Thus one has to be careful in extracting even relative reduced width information from multinucleon transfer reactions.

The present $E2$ data are analyzed based on a microscopic cluster model capture calculation rather than R -matrix formalism, since the latter would introduce a large number of free parameters (three for each 2^+ level) for very few data points. In our analysis the potential between the alpha particle and the ^{12}C is assumed to be of Gaussian shape

$$V(r) = V_0 e^{-r^2/r_0^2}. \quad (25)$$

The value of r_0 is fixed at 2.8 fm and V_0 is varied to fit the $E2$ capture data. The best fit to our data gives $S_{E2}(300) = 36 \pm 6$ keV b.

Only one other experiment, that of Redder *et al.* [4], measured the angular distribution of the $^{12}\text{C}(\alpha,\gamma)^{16}\text{O}$ reaction over a sufficient energy range to allow for an accurate separation of the $E1$ and $E2$ amplitudes. Our data are in good agreement with their results as shown in Fig. 13(b). When the cluster model is used to fit data from both experiments, it yields $S_{E2}(300) = 31 \pm 6$ keV b. The fitting is rather poor with

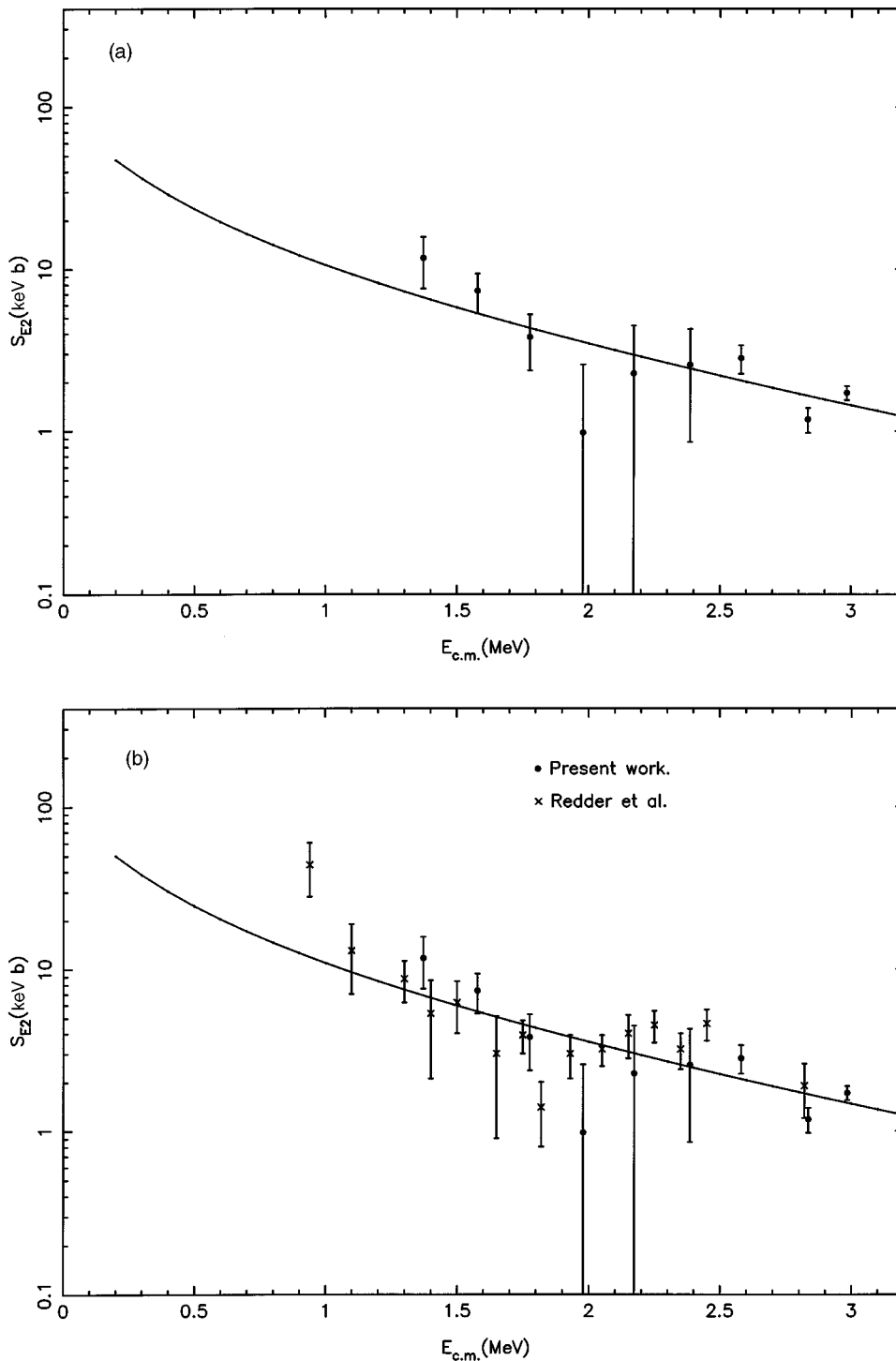


FIG. 13. (a) The $E2$ astrophysical S factor from the present work. The curve is from the best fit to a cluster model. (b) The $E2$ astrophysical S factor from the present work and the data of Redder *et al.* [4]. The curve is from the best fit to the combined data excluding the point of Redder *et al.* at 1.84 MeV.

a reduced χ^2 of 2.0. Most of the χ^2 comes from Redder's datum at 1.84 MeV, which deviates significantly from the nearby data. If that point is removed, the result is $S_{E2}(300) = 38 \pm 6$ keV b with a reduced χ^2 of 1.2. This is in good agreement with the value of $S_{E2}(300) = 50$ keV b deduced by Redder *et al.* [4] who used a cluster model fitting procedure which did not take into account that the calculated direct capture rate to the 6.92-MeV state is less than the value deduced from their data. Other microscopic calculations [23,29,30] generally give larger $S_{E2}(300)$ in the range 70–90 keV b.

The ^{16}N β decay does not populate the subthreshold 2^+

level. Information on its alpha width comes from $l=2$ phase shift analysis of elastic scattering data [5], (α, γ) capture, and alpha transfer reactions [28]. Redder *et al.* [4] used $l=2$ phase shift analysis to deduce a reduced α width of $\theta^2(6.92) = 0.34 \pm 0.15$, from which they obtained $S_{E2}(300) = 89 \pm 30$ keV b using a simple single-level calculation. This was done by fitting the small negative phase shift below the broad 2^+ resonance ($\Gamma = 75$ keV) at $E_\alpha = 5.81$ MeV over the energy range $E_\alpha = 2-5$ MeV, right in the region of a sharp 2^+ resonance ($\Gamma = 1$ keV), which is not shown in the data. The fit is quite poor above 6 MeV where the measurements would favor a smaller value for $\theta^2(6.92)$. They also

analyzed their $E2$ capture data using the R -matrix formalism and deduced a value of $\theta^2(6.92)$ in the range of 0.07–0.72. The large uncertainty is due in part to the difficulty of separating the contributions from the 2^+ subthreshold state and direct capture. When they include the analysis of the data for the cascade transitions via the 6.2-MeV level, the error in the alpha width is reduced and they obtain a reduced α width of $\theta^2(6.92)=0.39\pm 0.20$, in agreement with elastic scattering analysis. This gives an $E2$ S factor of $S_{E2}(300)=96^{+24}_{-30}$ keV b, which is in good agreement with the acceptable range of 50–180 keV b obtained by Barker and Kajino [31] using R -matrix analysis constrained by cascade transitions. The rather large uncertainty is a consequence of the large number of parameters used in their fitting procedure. Humblet *et al.* [19] reanalyzed the published data of Plaga *et al.* [5] and Redder *et al.* [4] using a K -matrix formalism. They obtained a good fit to the phase shift below and above the broad 2^+ resonance and deduced a small value for the $E2$ S factor $S_{E2}(300)=7^{+24}_{-6}$ keV b.

Other than the theoretical question [11] of whether a subthreshold echo pole is allowed or not in the K -matrix formalism, both the K -matrix and R -matrix analyses of the $^{12}\text{C}(\alpha,\gamma)^{16}\text{O}$, $^{12}\text{C}(\alpha,\alpha)^{16}\text{C}$, and ^{16}N β decay give consistent extrapolated values of the $E1$ capture S factor in the neighborhood of 80 keV b. The error is harder to estimate because of the systematic differences in each (α,γ) data set. As discussed earlier in Sec. IV A and IV B, an uncertainty of ± 15 keV b is not an unreasonable value. So the $E1$ S factor is now known to about 20%.

The situation with the $E2$ capture rate is not as well established. Without a direct measurement of the alpha width of the 2^+ level at 6.9 MeV, it is difficult to obtain a reliable extrapolation of the $E2$ S factor from existing data. Unfortunately, reduced widths from multinucleon transfer experi-

ments are not reliable. Fitting to the elastic scattering phase shift and $E2$ capture data with different models produce very different values for S_{E2} , in the range 7–95 keV b. It is interesting to note that for different analyses which look at the combined $E1$ and $E2$ data [4,18,30,23,31], while the deduced values of $S_{E1}(300)$ may differ by factors of 4 or more, in almost all cases the deduced value of $S_{E2}(300)$ is a factor of 2 smaller than the deduced $S_{E1}(300)$. It appears that any analysis which overestimates $S_{E1}(300)$ also give a large value of $S_{E2}(300)$. With $S_{E1}(300)$ now fixed at about 80 keV b, the best estimate of $S_{E2}(300)$ would appear to be about 40 keV b, the value deduced from cluster model analysis. It would be unrealistic to consider the uncertainty derived in that analysis to be a good estimate of the uncertainty in S_{E2} since the model itself strongly constrains the extrapolation. However, it would appear to be unlikely that $S_{E2}(300)$ would fall outside the range of 10–70 keV b if we scale the published values of $S_{E2}(300)$ in each paper by adjusting the corresponding $S_{E1}(300)$ values to 80 keV b.

The best estimate of the value of the total S factor for the $^{12}\text{C}(\alpha,\gamma)^{16}\text{O}$ reaction at $E_{\text{c.m.}}=300$ keV is $S(300)=120$ keV b. The uncertainty of $S(300)$ is hard to estimate because of theoretical difficulties. It would be unlikely for $S(300)$ to fall outside the range of 80–160 keV b. The 30% uncertainty in the total S factor is dominated by the large error assigned to $S_{E2}(300)$. This large uncertainty is a reflection of the large variation in the extrapolations using different reaction models. It can be reduced substantially by improvements in theories for multinucleon transfer reactions and a better understanding of why the R -matrix and K -matrix analyses give such large differences in the extrapolated $S_{E2}(300)$.

This work was supported by the Natural Sciences and Engineering Research Council of Canada.

-
- [1] W. A. Fowler, *Rev. Mod. Phys.* **56**, 149 (1984).
 [2] T. A. Weaver and S. E. Woosley, *Phys. Rep.* **227**, 65 (1993).
 [3] C. E. Rolfs and W. S. Rodney, *Cauldrons in the Cosmos* (University of Chicago Press, Chicago, 1988), p. 387.
 [4] A. Redder, H. W. Becker, C. Rolfs, H. P. Trautvetter, T. R. Donoghue, T. C. Rinckel, J. W. Hammer, and K. Langanke, *Nucl. Phys.* **A462**, 385 (1987).
 [5] R. Plaga, H. W. Becker, A. Redder, C. Rolfs, H. P. Trautvetter, and K. Langanke, *Nucl. Phys.* **A465**, 291 (1987).
 [6] P. Dyer and C. A. Barnes, *Nucl. Phys.* **233**, 495 (1974).
 [7] K. U. Kettner, H. W. Becker, L. Buchmann, J. Görres, H. Kräwinkel, C. Rolfs, P. Schmalbrock, H. P. Trautvetter, and A. Vlieks, *Z. Phys. A* **308**, 73 (1982).
 [8] R. M. Kremer, C. A. Barnes, K. H. Chang, H. C. Evans, B. W. Filippone, K. H. Hahn, and L. W. Mitchell, *Phys. Rev. Lett.* **60**, 1475 (1988).
 [9] J. M. L. Ouellet, H. C. Evans, H. W. Lee, J. R. Leslie, J. D. MacArthur, W. McLatchie, H.-B. Mak, P. Skensved, J. L. Whitton, X. Zhao, and T. K. Alexander, *Phys. Rev. Lett.* **69**, 1896 (1992).
 [10] R. E. Azuma, L. Buchmann, F. C. Barker, C. A. Barnes, J. M. D'Auria, M. Domsbky, U. Giesen, K. P. Jackson, J. D. King, R. G. Korteling, P. McNeely, J. Powell, G. Roy, J. Vincent, T. R. Wang, S. S. M. Wong, and P. R. Wrean, *Phys. Rev. C* **50**, 1194 (1994).
 [11] F. C. Barker, *Phys. Rev. C* **50**, 2244 (1994).
 [12] L. R. Doolittle, *Nucl. Instrum. Methods B* **9**, 344 (1985).
 [13] A. Anttila, J. Keinonen, M. Hautala, and I. Forsblom, *Nucl. Instrum. Methods* **147**, 501 (1977).
 [14] P. M. Endt, *Nucl. Phys.* **A521**, 1 (1990).
 [15] L. C. Northcliffe and R. F. Schilling, *Nucl. Data Tables A* **7**, 233 (1970).
 [16] P. R. Bevington, *Data Reduction and Error Analysis for the Physical Sciences* (McGraw-Hill, New York, 1969), p. 142.
 [17] F. Ajzenberg-Selove, *Nucl. Phys.* **A460**, 1 (1986).
 [18] J. Humblet, P. Dyer, and B. A. Zimmerman, *Nucl. Phys.* **A271**, 210 (1976); B. W. Filippone, J. Humblet, and K. Langanke, *Phys. Rev. C* **40**, 515 (1989).
 [19] J. Humblet, B. W. Filippone, and S. E. Koonin, *Phys. Rev. C* **44**, 2530 (1991); **48**, 2114 (1993).
 [20] F. James and M. Roos, "MINUIT: Function Minimization and Error Analysis," CERN Program Library D506 (unpublished).
 [21] A. M. Lane and R. G. Thomas, *Rev. Mod. Phys.* **30**, 257 (1958).

- [22] F. C. Barker, *Aust. J. Phys.* **25**, 341 (1972).
- [23] K. Langanke and S. E. Koonin, *Nucl. Phys.* **A410**, 334 (1983); **A439**, 384 (1985).
- [24] Y. Suzuki, *Prog. Theor. Phys.* **56**, 111 (1976).
- [25] S. Okabe, *Nucl. Phys.* **A404**, 179 (1983).
- [26] X. Zhao, H.-B. Mak, B. Castel, and J. R. Leslie, Report on Research in Nuclear Physics at Queen's University, 1986, p. 33; and (private communication).
- [27] Z. Zhao, R. H. France III, K. S. Lai, S. L. Rugari, and M. Gai, *Phys. Rev. Lett.* **70**, 2066 (1993).
- [28] F. D. Becchetti, D. Overway, J. Jänecke, and W. W. Jacobs, *Nucl. Phys.* **A344**, 336 (1980).
- [29] P. Descouvemont, *Phys. Rev. C* **47**, 210 (1993).
- [30] P. Descouvemont and D. Baye, *Phys. Rev. C* **36**, 1249 (1987).
- [31] F. C. Barker and T. Kajino, *Aust. J. Phys.* **44**, 369 (1991).